Insight into the interface properties of c-TiAl/a2-Ti3Al with La doping obtained by first-principles calculations

Qizhen He,[a] Chunmei Zhao,*[a] Wenwei Song,[a] Silong Zhang,[b] Zhijun Shi,[c] Xuejun Ren[d] and Qingxiang Yang[a]

[a] State Key Laboratory of Metastable Materials Science & Technology, Hebei key lab for optimizing metal product technology and performance, Yanshan University, Qinhuangdao, 066004, P. R. China. E-mail: zcmcl@ysu.edu.cn, qxyang@ysu.edu.cn; Fax: +86-335-807-4545; Tel: +86-335-838-7471
[b] Key Laboratory of Marine Materials and Related Technologies, Zhejiang Key Laboratory of Marine Materials and Protective Technologies, Ningbo Institute of Materials Technology and Engineering, Chinese Academy of Sciences, Ningbo, 315201, P. R. China
[c] School of Mechanical Engineering university, Yanshan University, Qinhuangdao, 066004, P. R. China
[d] School of Engineering, Liverpool John Moores University, Liverpool, L3 3AF, UK

Abstract:

The interface strength between TiAl and γ_2-Ti_3Al phases is pivotal for influencing the room temperature ductility of TiAl alloys. However, it is difficult to elucidate the bonding mechanisms of the γ-TiAl/α_2-Ti_3Al interface experimentally. The effects of La doping on the properties of the γ-TiAl/α_2-Ti_3Al interface were investigated by using first-principles calculations in this study. The energy stability of various atoms surrounding the interface following the substitution of La atoms was calculated and a model of the γ-TiAl/α_2-Ti_3Al interface was constructed. Meanwhile, the stability and electronic structure of the interface both before and after La doping were examined. The results demonstrate that the energy of the γ-TiAl/α_2-Ti_3Al interface model reaches its minimum when the Al atom at the Doped 5 site is substituted by a La atom. The interface binding energies for the clear and doped models are determined to be 3.86 J m^{-2} and 2.47 J m^{-2}, respectively. Similarly, the corresponding interface energies are found to be 1.65 J m^{-2} and 1.15 J m^{-2}. The charge analysis of the interface models reveals that the primary bonding at both interface types consists of Ti–Ti and Ti–Al bonds. In the doped interface, the La atom doping results in the formation of La–Al bonds. The results from the tensile tests reveal that the tensile stresses for the undoped and doped interface models are 19.18 GPa and 11.26 GPa, respectively. The potential energy surface analysis demonstrates that the maximum potential energy values for the clear and doped interfaces are 1.605 J m^{-2} and 0.816 J m^{-2}, respectively. Along the minimum energy path, the energy barriers for heterogeneous sliding at the interfaces are determined to be 0.404 J m^{-2} and 0.243 J m^{-2}, while the ideal shear strengths are 0.286 GPa and 0.130 GPa, respectively. Therefore, the doping of La atoms enhances the ductility of the γ-TiAl/α_2-Ti_3Al interface.

1. Introduction

TiAl alloys possess numerous advantages, such as low density, high specific strength, high specific stiffness, and exceptional resistance to high-temperature oxidation and creep. These properties enable them to be widely applied in both aerospace and civilian industries.[1–3] However, their poor ductility at room temperature and considerable brittleness significantly constrain their applicability.[4–6] In TiAl alloys, γ-TiAl and α_2-Ti_3Al are the primary phases.[7] The interface strength between TiAl and γ_2-Ti_3Al phases is pivotal for influencing the room temperature ductility of TiAl alloys.8 Therefore, it is significant to improve the interface strength between γ-TiAl and α_2-Ti_3Al phases for broadening the application fields of TiAl alloys. In recent years, many research studies have been conducted on improving the mechanical properties of TiAl alloys by the alloying method.[9–11] Zhang et al.[12] found that the Nb addition can induce the formation of anti-site atomic defects, which contribute to solid solution strengthening and elevate the critical shear stress for dislocation slip. Meanwhile, the Nb addition can decrease the stacking fault energy of TiAl-based alloys and foster the generation of the deformation twins within the g phase. The presence of twin boundaries impedes dislocation movement, which can improve the plastic deformation capabilities of TiAl-based alloys. Lin et al.[13] elucidated that the Nb addition in TiAl alloys can lower the critical Al content necessary for forming external Al_2O_3 oxide films, which consequently inhibits further oxidation reactions. Moreover, Ti_4+ in TiO_2 can be substituted by Nb^{5+}, which leads to a reduction in vacancy concentration and a decreased oxidation reaction rate, which enhances the oxidation resistance of TiAl alloys. Kim et al.[14] investigated the effects of adding C and Si to TiAl alloys and found that their incorporation results in the precipitation of incongruent H-type carbides (Ti_2AlC) and silicides (Ti_5Si_3) at the lamellar interfaces. These precipitates hinder dislocation motion, reduce the deformation during the primary stage of creep, and suppress or slow down the third stage of creep, which lead to enhancement of the high temperature creep resistance of the alloy. These research stu dies suggest that alloying can improve the mechanical proper ties of TiAl alloys to some extent; however, the poor ductility of TiAl alloys still persists.

Rare earth elements are widely used as strengthening agents for both ferrous and non-ferrous metals.[15,16] The addition of rare earth elements to alloys results in grain refinement, solid solution strengthening, and purification effects, which significantly improve the mechanical properties of the alloys.[17–19] Guo et al.[20] investigated the effects of Y_2O_3 on the high-temperature tensile properties and fracture behavior of the Ti–48Al 2Cr–2Nb alloy. The Y_2O_3 addition led to a notable increase in the tensile strength and elongation of the TiAl alloy. Additionally, Y_2O_3 effectively impedes dislocation movement and promotes the nucleation of deformation twins during tensile testing. Morteza[21] investigated the effects of La on the microstructure and high temperature mechanical

properties of a TiAl alloy. It was found that the addition of 0.2 at% La facilitates the formation of fine oxide particles within the alloy, as La combined with O to create these particles. These particles are dispersed throughout the alloy and act as a dispersion strengthening agent. Additionally, they delayed dynamic recrystallization during thermal deformation. Therefore, it is inferred that the doping of rare earth atoms in TiAl alloys results in a certain improvement in their properties. However, it is hard to elucidate the mechanism of the interface interaction between the γ-TiAl and α_2-Ti_3Al phases in TiAl alloys by experimental methods.

Recently, first-principles methods based on density functional theory have emerged as crucial tools for exploring the surface and interface properties of materials.[22–24] Rao et al.[25] utilized first-principles techniques to compute the binding energy and differential charge density of the TiN(111)/diamond(111) interface before and after relaxation. They demonstrated that post-relaxation the interface binding energy is decreased due to the graphitization of the diamond. Additionally, the electrostatic interactions among the atoms at the interface are changed, which leads to a reduction in the bonding strength of the interface. Chen et al.[26] conducted high-throughput first principles calculations on the binding energies of 468 different $NiTi_2/Al_2O_3$ interfaces and identified eight interface configurations with relatively high binding strengths, which are categorized as metal–metal and metal–oxide interfaces. Tensile simulations indicate that the tensile strength of the metal–oxide interfaces exceeds 10 GPa, while that of the metal–metal interfaces is below this value. In all the examined metal–metal and metal–oxide interfaces, fracture always occurs near the $NiTi_2$ phase at the interface. Therefore, it is feasible to use first principles methods to explain the effect of rare earth atom doping on the interface interactions between γ-TiAl and α_2 Ti_3Al phases in TiAl alloys. The dual-phase TiAl alloy with γ-TiAl and α_2-Ti_3Al phases was taken in this study. A γ-TiAl/α_2-Ti_3Al interface model was constructed and the rare earth element lanthanum (La) was selected as the doping agent. The stability and electronic structure of the interface both before and after doping were calculated. Meanwhile, the tensile simulations on the interfaces before and after doping were performed and the potential energy surfaces for both interfaces were computed to obtain the minimized energy paths for interface slip and the ideal shear strength. They can reveal the impact of La atom doping on the properties of the γ-TiAl/α_2-Ti_3Al interface, which can provide a theoretical foundation for future improvements in the mechanical properties of dual-phase TiAl alloys by the rare earth alloying method.

2. Computational method

All calculations in this study were performed by using the Vienna ab initio simulation package (VASP) based on density functional theory (DFT)[27] and the projector augmented wave (PAW) method.[28] The exchange–correlation potential was calculated by using the generalized gradient approximation (GGA) with Perdew–Burke–Ernzerhof (PBE) parameters.[29] During the geometry optimization process, all atomic positions were allowed to relax freely until the total energy and forces con verged to 10^{-5} eV $atom^{-1}$ and 0.001 eV $Å^{-1}$, respectively. The Monkhorst–Pack scheme[30] was employed to sample the irreducible Brillouin zone (IBZ) with a K-point grid. The convergence criteria were set with an energy convergence threshold of $1.0x10^{-5}$ eV and a Hellmann–Feynman force convergence of 0.02 eV per atom. Convergence tests for the selected structures encut and K-points were conducted to ensure the accuracy of the calculations. The variations in energy with respect to encut and K-points for g-TiAl and a2-Ti3Al are shown in Fig. 1. Based on these results, the specific parameters for the encut and K-point selection for the bulk, surface and interface models are detailed in Table 1.

3. Results and discussion

3.1 Determination of interface relationship between γ-TiAl and α_2-Ti_3Al

Before calculating the surface properties of γ-TiAl and α_2-Ti_3Al, it is essential to fully relax the bulk structures of γ-TiAl and α_2-Ti_3Al to achieve their most stable states. The crystal structures of fully relaxed γ-TiAl and α_2-Ti_3Al are illustrated in Fig. 2. Fig. 2(a) displays the crystal structure of γ-TiAl, which belongs to the space group P4/MMM. After thorough relaxation, the calculated lattice constants are a = b = 3.999 Å and c = 4.042 Å, values that are in close agreement with those obtained experimentally[31] and computationally.[32] Fig. 2(b) displays the crystal structure of α_2-Ti_3Al, which belongs to the P63/MMC space group. After relaxation, its lattice constants are determined to be a=b=5.742Åandc=4.646Å, which are consistent with values obtained experimentally33 and computationally.[34] These results demonstrate the accuracy of the γ-TiAl and α_2 Ti_3Al unit cells utilized in this study, which have been widely adopted in other works and yielded reasonable outcomes, thereby meeting the computational requirements of this study.

Based on previous research findings,[35–37] an interface model was constructed by using the γ-TiAl(111) crystal plane and the α_2-Ti_3Al(0001) crystal plane. Before constructing the interface model, it was necessary to determine the optimal layer thick ness for the surface models of γ-TiAl and α_2-Ti_3Al. The surface models of γ-TiAl(111) and α_2-Ti_3Al(0001) with varying thicknesses were built, and convergence tests of the surface energies of both models were conducted to ascertain the minimum number of layers required to achieve properties representative of the bulk phase. A 15 Å vacuum layer was added in both the surface models and subsequent interface models to mitigate interactions between the

surface layers under periodic boundary conditions. The results of the surface models for the γ-TiAl(111) and α_2-Ti_3Al(0001) crystal planes are shown in Fig. 3.

The surface energies of the two surface models can be calculated using the Botteger formula:[38]

$$\sigma = \frac{1}{2A}\left(E_{\text{slab}}^{N} - N\Delta E\right) \qquad (1)$$

$$\Delta E = \left(E_{\text{slab}}^{N} - E_{\text{slab}}^{N-2}\right)/2 \qquad (2)$$

where s denotes the surface energy of the model; E_{slab}^{N} and E_{slab}^{N-2} indicate the total energy of the surface models containing N layers and N2 layers of atoms, respectively; and A represents the surface area of the model.

The calculation results of the surface energy of γ-TiAl(111) and α_2-Ti3Al(0001) crystal planes are shown in Table 2, which indicates that when the number of surface layers is larger than 6, the energy converges to 3.47 J m^{-2} for γ-TiAl(111), and when the number of surface layers is larger than 7, the energy converges to 2.04 J m^{-2} for α2-Ti3Al(0001) interfaces.

Based on the surface model calculations where the number of γ-TiAl surface layers is 6 and that of α2-Ti3Al surface layers is 7, two different interfacial models are constructed. For the γ-TiAl/α_2-Ti_3Al interface, there are two distinct interfacial models primarily distinguished by whether the pure Ti atomic columns align when crossing the interface. Due to the different arrangements of Ti/Al atoms near the two types of interfaces, it is inevitable that one interface will have a lower energy. The calculations reveal that the interface energy where the pure Ti atomic columns align is lower, compared to the case where they do not align, consistent with the results in the literature.[39] Therefore, only the case where the pure Ti atomic columns align in our subsequent calculations has been considered. The γ-TiAl/α_2-Ti_3Al interfacial model is shown in Fig. 4.

In the process of constructing the interfacial model, the optimal interfacial spacing was determined by analyzing the correlation between interfacial spacing and structural energy. On this basis, the relaxation and energy calculations were conducted on interfacial models with spacings ranging from 1.0 to 4.0 Å, incremented by 0.1 Å. As shown in Fig. 5, the relationship between the variation in interfacial energy and spacing is clearly illustrated. Notably, the interfacial structure exhibits its lowest energy at a spacing of 2.3 Å, which signifies the most favorable atomic interactions near the interface. Consequently, the optimal interfacial spacing is identified as 2.3 Å.

To ensure the stability of the structure after doping, eight positions were selected for replacement at the interface and on both sides of the interface based on the constructed interfacial model, as shown in Fig. 6. Fig. 6(a) and (b) show the substitution points for the doped atoms at the interface and sub- interface, respectively, with α_2-Ti_3Al located above the interface and g-TiAl below. Subsequently, the energy calculations were performed and compared for each position, as depicted in Fig. 6(c). It can be observed that the interfacial model energy is generally higher when La atoms occupy Ti positions compared to when they occupy Al positions. Therefore, La atoms tend to occupy positions originally occupied by Al positions. Specifically, the lowest energy configuration occurs when La occupies the Al position at the interface Doped 5 (the Al position on the α_2-Ti_3Al side). Consequently, this interfacial model is selected for subsequent calculations. The doped interface model and the undoped interface model are referred to as the doped interface and clear interface, respectively.

3.2 Stability testing of the interface mode

The interface stability can be analyzed using work of separation (W_{sep}) and interface energy (γ). W_{sep} is a significant parameter that characterizes the strength of the interfacial bonding. It represents the reversible work required to separate the interface into two free surfaces and disregard the effects of the plastic deformation and diffusive degrees of freedom. A larger value of W_{sep} indicates a stronger ideal interfacial bond, which can be used to approximate the bonding strength of the interface structure. Specifically, a higher W_{sep} suggests that more energy is required to disrupt the interfacial structure. The calculational formula for W_{sep} is as follows:[40]

$$W_{sep} = \frac{E_{\gamma-TiAl} + E_{\alpha_2-Ti_3Al} - E_{\gamma-TiAl/\alpha_2-Ti_3Al}}{A} \qquad (3)$$

For the doped interface, the calculation formula is as follows:

$$W_{sep} = \frac{E_{\gamma\text{-}TiAl} + E_{\alpha_2\text{-}Ti_3Al-La} - E_{\gamma\text{-}TiAl/\alpha_2\text{-}Ti_3Al-La}}{A} \qquad (4)$$

where $E_{\gamma\text{-}TiAl}$ and $E_{\alpha2\text{-}Ti3Al}$ are the total energies of 6 layer g-TiAl and 7 layer α_2-Ti3Al surface models; $E_{\gamma\text{-}TiAl/a2\text{-}Ti3Al}$ is the total energy of the clear interface model; $E_{\alpha2\text{-}Ti3Al–La}$ is the total energy of the surface model after the La atom replacing the Al atom; $E_{\gamma\text{-}TiAl/a2\text{-}Ti3Al–La}$ is the total energy of the doped interface model; and A is the interfacial area.

Another criterion for interface stability is interfacial energy g. γ can be considered as the resistance encountered when two bulk materials form a heterogeneous interface structure,[41] and it plays a crucial role in nucleation processes. The magnitude of g corresponds to the difficulty of the heterogeneous nucleation at the interface. Generally, a smaller γ indicates that the interface structure is more likely to form. The calculation formula for g is as follows:[42]

$$\gamma = \sigma_{\gamma\text{-TiAl}} + \sigma_{\alpha_2\text{-Ti}_3\text{Al}} - W_{sep} \quad (5)$$

For a doped interface, the calculation formula is as follows:

$$\gamma = \sigma_{\gamma\text{-TiAl}} + \sigma_{\alpha_2\text{-Ti}_3\text{Al-La}} - W_{sep} \quad (6)$$

where W_{sep} is the work of separation of the clear interface structure and $\sigma_{\gamma\text{-TiAl}}$ and $\sigma_{\alpha 2\text{-Ti3Al–La}}$ are the surface energies of the γ-TiAl and La-doped α_2-Ti_3Al layers, respectively.

The surface energy of the La-doped α_2-Ti_3Al layer, denoted as $\sigma_{\alpha 2\text{-Ti3Al–La}}$, is calculated using the following formula:

$$\sigma_{\alpha_2\text{-Ti}_3\text{Al-La}} = \frac{1}{2A}[E_{slab} - N_{Al}\mu_{Al} - N_{Ti}\mu_{Ti} - N_{La}\mu_{La}] \quad (7)$$

where $\sigma_{\alpha 2\text{-Ti3Al–La}}$ is the surface energy of the model; E_{slab} is the total energy of the La-doped surface model, expressed as α_2-Ti_3Al–La; N_{Al}, N_{Ti} and N_{La} are the number of Al, Ti, and La atoms in the surface model, respectively; μ_{Al} and μ_{Ti} are the chemical potentials of Al and Ti in α_2-Ti_3Al; and μ_{La} is approximately equal to the chemical potential of La atoms in the bulk phase structure.

For the α2-Ti3Al bulk unit cell, the calculation formula is as follows:

$$\mu^{bulk}_{\alpha_2-\text{Ti}_3\text{Al}} = 3\mu_{Ti} + \mu_{Al} \quad (8)$$

Combining formulas (7) and (8), the approximate condition results in a surface energy value of $\sigma_{a2\text{-Ti3Al–La}} = 0.15\ J\ m^{-2}$.

The W_{sep} and γ of the interface models are presented in Table 3. It is evident that the doped interface is more conducive to formation compared to the clear interface. However, the clear interface exhibits a higher bonding strength. This suggests that La atoms are more likely to reside at grain boundaries, which reduces interfacial bonding strength, thereby enhancing the ductility of the interface.

3.3 Bonding properties of the interface

The electronic structure and bonding characteristics of the interface can reflect the interface properties, which can be evaluated using differential charge density.43 The differential charge density diagrams of the γ-TiAl/a_2-Ti3Al interface model are shown in Fig. 7. Among them, Fig. 7(a) and (b) are the 3D differential charge density diagram and 2D differential charge density diagram of the clear interface, respectively.

As shown in Fig. 7(a), the charges gather from both sides of the interface to the center, with charges more inclined towards Ti atoms. Combining with the 2D differential charge density diagram in Fig. 7(b), it can be observed that there is an obvious charge

accumulation area near the interface, mainly around the Ti atoms. There are evident charge depletion areas at positions far from the interface, which proves that there is a significant bonding effect between the atoms above and below the interface. There is a charge dissipation phenomenon between the Ti atoms above and below the interface, and Ti has a stronger electronegativity, which can cause electrons to concentrate near the interface to form a charge accumulation area. A significant diffusion phenomenon occurs in both layers of atoms near the interface, which form Ti–Al bonds and Ti–Ti bonds on both sides of the interface. To analyze the charge transfer situation of the interface more directly, the planar averaged charge transfer along the z-axis for the clear interface in the γ-TiAl/ α_2-Ti3Al interface model was studied, as shown in Fig. 7(c). It can be clearly seen that there is an obvious charge transfer in the range of 10–18 Å in the Z direction, with a value of 0.53e , which is consistent with the above differential charge density performance. This indicates that there is a significant bonding characteristic near the interface.

The differential charge density diagrams of the doped interface of the γ-TiAl/α_2-Ti_3Al interface model are shown in Fig. 7(d) and (e). Among them, Fig. 7(d) is the 3D differential charge density diagram of the doped interface. It can be seen that charges also gather from both sides of the interface to the center, with charges more inclined towards the Ti atoms on the α_2-Ti_3Al side. A significant charge transfer phenomenon occurs at the La atoms above the interface. Combining with the 2D differential charge density diagram in Fig. 7(e), it can be observed that there is an obvious charge accumulation area near the interface, mainly around the Ti atoms. There are evident charge depletion areas at positions far from the interface, which prove that there is a significant bonding effect between the atoms above and below the interface. There is a charge dissipation phenomenon between the Ti atoms above and below the interface, and there is a charge depletion area near the La atoms on the α_2-Ti_3Al side, which indicates that both Ti and La have strong electronegativity and cause electrons to concentrate near the interface to form a charge accumulation area. A significant diffusion phenomenon occurs in both layers of atoms near the interface, which form Ti–Al bonds, Ti–Ti bonds and La–Al bonds on both sides of the interface. Fig. 7(f) illustrates the planar averaged charge trans fer along the z-axis for the doped interface in the γ-TiAl/a_2-Ti_3Al interface model. It can be clearly seen that there is an obvious charge transfer in the range of 10–18 Å in the Z direction, with a value of 0.51e , which is consistent with the above differential charge density performance. This indicates that there is a significant bonding characteristic near the interface.

The electron localization function (ELF) can be employed to qualitatively characterize the localized distribution of electrons and aid in verifying bond types. The calculation formula for the ELF is as follows:[44]

$$\mathrm{ELF} = 1 \Big/ \left[1 + \left(\frac{D(r)}{\mathrm{Dh}(r)}\right)^2\right] \qquad (9)$$

where D(r) is the real electron gas density and Dh(r) is the uniform electron gas density.

The ELF values range from 0 to 1. When ELF = 1, the electrons are completely localized. When ELF = 1/2, the electrons are in a homogeneous electron gas state. When ELF = 0, the electrons are completely delocalized (or absent in this context).

The ELF distribution diagrams for the γ-TiAl/α_2-Ti_3Al interface model before and after doping are shown in Fig. 8. Fig. 8(a) is the clear interface. It can be observed that the ELF value for Ti atoms at the interface junction is about 0.8, which is gradually decreased outward from the Ti atoms, with the outer most ELF value being approximately 0.2. This indicates that electrons move closer to Ti atoms and result in localized electron states near the Ti atoms, which suggest the formation of Ti–Ti metallic bonds near the interface. The ELF values around Al atoms below the interface are about 0.5, which indicates that electrons around these Al atoms are in a homogeneous electron gas state. The ELF values around Al atoms far from the interface approach 0, which indicates that there are almost no electrons around them. Fig. 8(b) shows the doped interface. Compared to the clear interface, the bonding states of Ti and Al atoms on both sides of the interface are similar. However, it is noteworthy that the ELF value for La atoms on the α_2-Ti_3Al side is about 0.85 and is gradually decreased, which indicates the formation of La–Al covalent bonds near the interface.

The density of states (DOS) analysis45 is a fundamental method to investigate the electronic structure of materials. The partial density of states (PDOS) analysis of the γ-TiAl/α_2Ti_3Al interface is shown in Fig. 9. Fig. 9(a) shows the PDOS of the clear interface. It is evident that the d-orbitals of Ti atoms are the predominant contributors to the peaks in the total density of states. The presence of non-zero density of states at the Fermi level indicates that the chemical bonds formed at the interface exhibit metallic characteristics. Specifically, within the energy range from -1 eV to the Fermi level, the p orbital of Ti atoms above the interface and the s orbital of Ti atoms below the interface show consistent peak shapes and similar peak values, which suggest the formation of Ti–Ti metallic bonds near the interface. In the energy range of -3 eV to -1 eV, the p orbital of Ti atoms above the interface resonates with the p orbital of Al atoms, and their peak shapes are consistent, which indicates the formation of Ti–Al metallic bonds. These observations collectively indicate that the bonding at the interface is primarily composed of both Ti–Ti and Ti–Al metallic bonds. Fig. 9(b) shows the PDOS of the doped interface. It is observed that the d-orbitals of Ti atoms contribute most significantly to the peaks in the total density of states peaks, and a distinct peak in the density of states at the Fermi level indicates the formation of metallic bonds. Near the interface, the p orbital of Ti atoms above the interface and the s orbital of Ti atoms below the interface exhibit consistent peak shapes and similar peak values, which confirm the formation of Ti–Ti metallic bonds. In the

energy range of -3eVto -1 eV, the s orbital of La atoms above the interface exhibits resonance and hybridization with the p-orbitals of Al atoms, and their peak shapes are consistent, which indicates the formation of La–Al covalent bonds. Additionally, the s orbital of Ti atoms above the interface and the p orbital of Al atoms show consistent peak shapes, which indicates the formation of Ti–Al metallic bonds. Consequently, the bonding types at the doped interface include Ti–Ti and Ti–Al metallic bonds, as well as La–Al covalent bonds.

3.4 Tensile and shear properties of the interface

To further analyze the interaction strength at the interface, the tensile simulations were conducted on the heterogeneous interface models. The tensile simulations were achieved by fixing the bottom and top atoms of the heterogeneous interface models and proportionally increasing the height of the models, meaning that engineering strain was applied in the z-axis direction with a step size of 1%. During the tensile simulations, atoms were allowed to freely relax in the z-axis direction only, disregarding Poisson's contraction in the direction parallel to the interface. The calculation formula for he stress–strain curves of the interface models is as follows:[46]

$$\varepsilon_{\text{tensile}} = \frac{l - l_0}{l_0} \tag{10}$$

$$\sigma_{\text{tensile}}(\varepsilon) = \frac{l + \varepsilon_{\text{tensile}}}{V(\varepsilon)} \frac{\partial E_{\text{total}}(\varepsilon)}{\partial \varepsilon_{\text{tensile}}} \tag{11}$$

where $\sigma_{tensile}$ is the tensile stress of the interface model; $\varepsilon_{tensile}$ is the tensile strain of the interface model; l_0 is the length of the interface model in the z-axis direction before stretching; l is the length of the interface model in the z-axis direction after stretching; $V(\varepsilon)$ stands for the volume of the interface model at a strain of ε; and $E_{total(\varepsilon)}$ is the total energy of the interface model at a strain of ε.

The deformation energy and tensile stress of both interface models as a function of the tensile strain are shown in Fig. 10. It can be observed that both interface models exhibit increasing strain energy and tensile stress with the increase of the tensile strain. At a strain of 18%, the tensile stress of the clear interface reaches its maximum at 19.18 GPa. Further stretching results in the tensile stress gradually approaching zero. Therefore, it can be concluded that after a strain of 18%, the bonding between atoms at the clear interface breaks, which causes the interface model to separate into two distinct surfaces. For the doped interface, it is apparent that the tensile stress reaches its maximum at a strain of 9%, with a value of 12.90 GPa. A com parison between the clear and doped interfaces reveals that the addition of La atoms augments the toughness of the interface. This observation underscores the beneficial impact of alloying elements on enhancing the mechanical integrity and resilience of the interface structures.

By comparing the sliding barriers at different positions of the heterogeneous interface models, it is possible to determine the preferred locations for relative sliding under shear forces. A grid of 11x11mesh points was selected within the interface models. Based on the chosen sliding positions and the mesh points, the relative positions for the two models were established, which results in a total of 121 interface models.

The calculation formula for the sliding potential energy (DE)is as follows:[47]

$$\Delta E = \frac{\left(E_{\mathrm{I}} - E_{\mathrm{I}}^{\min}\right)}{A} \qquad (12)$$

where E_I is the interaction energy of the interface model sliding to the current position; $E_{\mathrm{I}}^{\min}$ is the minimum interaction energy during the sliding process of the interface model; and A is the area of the interface model.

An in-depth analysis was conducted to assess the shear performance of the interface models before and after doping. The potential energy surfaces (PES) for sliding at the interface positions of the clear and doped models were computed. The direction denoted by the red dashed line represents the minimum energy path (MEP) required for heterogeneous sliding at the interface, corresponding to the lowest energy required for sliding along that path. By connecting all the sliding potential energies along this path, the potential energy curves (PECs) for the two heterogeneous interfaces were obtained. Differentiating these PECs yields dE/dl, where the maximum value of dE/dl signifies the ideal shear strength (τ_{MEP}) of the heterogeneous sliding interface along the minimum energy path, as illustrated in Fig. 11.

Fig. 11(a) and (b) present the sliding PES for the clear and doped interfaces, respectively. It is evident that the maximum potential energy values at the interface are 1.605 J m^{-2} and 0.816 J m^{-2}, respectively, indicating the energy barriers that must be overcome for relative sliding at the two different interface models. Fig. 11(c) and (d) present the PEC for the clear and doped interfaces along the MEP for sliding. The energy barriers for heterogeneous sliding at the MEP are 0.404 J m^{-2} and 0.243 J m^{-2} for the clear and doped interfaces, respectively. Fig. 11(e) and (f) present the differential values dE/dl for the PEC along the MEP for the clear and doped interfaces. The calculated (τ_{MEP}) values for the sliding interfaces of the clear and doped models are 0.286 GPa and 0.130 GPa, respectively. In summary, the doped interface exhibits a greater propensity for sliding compared to the clear interface, which suggests that doping with La atoms enhances the ductility of the interface.

4. Conclusions

(1) The surface energy convergence tests indicate that the surface models of γ-TiAl(111) and α_2-Ti_3Al(0001) achieve con vergence at 6 layers and 7 layers, respectively, with the corresponding surface energies of 3.47 J m^{-2} and 2.04 J m^{-2}.

(2) The interface energy is the lowest when the La atom occupies the Al position at the Doped 5 interface site. After full relaxation, the interfacial work of separation values for the clear interface model and the doped interface model are 3.86 J m^{-2} and 2.47 J m^{-2}, respectively. The clear interface develops Ti–Al and Ti–Ti bonds on both sides, while the doped interface forms Ti–Al, Ti–Ti, and La–Al bonds on both sides.

(3) From stretching calculations on the interface models, it is found that the maximum tensile stresses for the clear and doped interface models are 19.18 GPa and 11.26 GPa, respectively. This indicates that the incorporation of La atoms enhances the toughness of the interface.

(4) From potential energy surface calculations on the interface models, the maximum potential energy values for the clear and doped interface models are found to be 1.605 J m^{-2} and 0.816 J m^{-2}, respectively. The energy barriers for interface sliding along the minimum energy path are 0.404 J m^{-2} and 0.243 J m^{-2}, with ideal shear strengths (τ_{MEP}) of 2.032 GPa and 0.161 GPa, respectively. Consequently, the doping of La atoms in the interface enhances its ductility.

Data availability

Data will be made available upon request. Conflicts of interest There are no conflicts to declare.

Acknowledgements

The authors would like to express their gratitude for projects supported by the National Natural Science Foundation of China (No. 52371077) and the Innovative Funding Project for Doctoral Postgraduates of Hebei Province, China (No. CXZZBS2024055)

References

1 H. Jabbar, J. Monchoux, M. Thomas, F. Pyczak and A. Couret, Improvement of the creep properties of TiAl alloys densified by spark plasma sintering, Intermetallics, 2014, 46, 1–3.

2 H. Z. Niu, Y. J. Su, Y. S. Zhang, D. L. Zhang, J. W. Lu, W. Zhang and P. X. Zhang, Microstructural evolution and mechanical properties of a b-solidifying g-TiAl alloy densified by spark plasma sintering, Intermetallics, 2015, 66, 96–102.

3 Y.K.Kim,S.J. Youn, S. W. Kim, J. Hong andK. A.Lee, High temperature creep behavior of gamma Ti–48Al–2Cr–2Nb alloy additively manufactured by electron beam melting, Mater. Sci. Eng., A, 2019, 736, 138138.

4 Y. B. Ke, J. Z. Tao and H. P. Duan, Structure Determination of Er Doped Ti-Al-Nb Alloy by Neutron Diffraction Analysis, Materials, 2019, 12, 2243.

5 L. Wang, Y. L. Zhang, X. M. Hua, C. Shen, F. Li, Y. Huang and Y. H. Ding, Fabrication of g-TiAl intermetallic alloy using the twin-wire plasma arc additive manufacturing process: Microstructure evolution and mechanical proper ties, Mater. Sci. Eng., A, 2021, 812, 141056.

6 X. W. Liu, Z. L. Zhang, R. Sun, F. C. Liu, Z. T. Fan and H. Z. Niu, Microstructure and mechanical properties of beta TiAl alloys elaborated by spark plasma sintering, Intermetallics, 2014, 55, 177–183.

7 Y. Wei, Y. Zhang, H. B. Zhou, G. H. Lu and H. B. Xu, First principles investigation on shear deformation of a TiAl/ Ti3Al interface and effects of oxygen, Intermetallics, 2012, 22, 41–46.

8 Y.Wei, Y. Zhang, G. H. Lu and H.B. Xu, Effects of transition metals in a binary-phase TiAl–Ti3Al alloy: From site occupancy, interfacial energetics to mechanical properties, Inter metallics, 2012, 31, 105–113.

9 J. P. Lin, X. J. Xu, Y. L. Wang, S. F. He, X. P. Song and G. L. Chen, High temperature deformation behaviors of a high Nb containing TiAl alloy, Intermetallics, 2007, 15, 668–674.

10 Q. Wang, H. S. Ding, H. L. Zhang, R. R. Chen, J. J. Guo and H. Z. Fu, Influence of Mn addition on the microstructure and mechanical properties of a directionally solidified g-TiAl alloy, Mater. Charact., 2018, 137, 133–141.

11 M.G.Li,S.L.Xiao, Y. Y. Chen, L. J. Xu and J. Tian, The effect of boron addition on the high-temperature properties and microstructure evolution of high Nb containing TiAl alloys, Mater. Sci. Eng., A, 2018, 733, 190–198.

12 W. J. Zhang, S. C. Deevi and G. L. Chen, On the origin of superior high strength of Ti–45Al–10Nb alloys, Intermetal lics, 2002, 10, 403–406.

13 J. P. Lin, L. L. Zhao, G. Y. Li, L. Q. Zhang, X. P. Song, F. Ye and G. L. Chen, Effect of Nb on oxidation behavior of high Nb containing TiAl alloys, Intermetallics, 2011, 19, 131–136.

14 Y. W. Kim and S. L. Kim, Effects of microstructure and C and Si additions on elevated temperature creep and fatigue of gamma TiAl alloys, Intermetallics, 2014, 53, 92–101.

15 K. Xia, X. Wu and D. Song, Effects of Gd addition, lamellar spacing and loading direction on creep behaviour of a fully lamellar Ti–44Al–1Mn–2.5 Nb alloy, Acta Mater., 2004, 52, 841–849.

16 C.L.Wang, Y.Gao, Z.C.Zeng and Y.K.Fu, Effect of rare-earth on friction and wear properties of laser cladding Ni-based coatings on 6063Al, J. Alloys Compd., 2017, 727, 278–285.

17 Y. Y. Chen, F. T. Kong, J. C. Han, Z. Y. Chen and J. Tian, Influence of yttrium on microstructure, mechanical proper ties and deformability of Ti–43Al–9V alloy, Intermetallics, 2005, 13, 263–266.

18 J. F. Gou, Y. Wang, Y. K. Zhang, C. H. Wang and G. Wang, Dry sliding wear behavior of Fe–Cr–C–B hardfacing alloy modified with nano-CeO2 and its mechanisms of modification, Wear, 2021, 484, 203756.

19 S. P. Sharma, D. K. Dwivedi and P. K. Jain, Effect of La2O3 addition on the microstructure, hardness and abrasive wear behavior of flame sprayed Ni based coatings, Wear, 2009, 267, 853–859.

20 Y. F. Guo, S. L. Xiao, Y. Y. Chen, J. Tian, Z. Z. Zheng and L. J. Xu, High temperature tensile properties and fracture behavior of Y2O3-bearing Ti–48Al–2Cr–2Nb alloy, Intermetallics, 2020, 126, 106933.

21 M. Hadi, M. Meratian and A. Shafyei, The effect of lanthanum on the microstructure and high temperature mechanical properties of a beta-solidifying TiAl alloy, J. Alloys Compd., 2015, 618, 27–32.

22 Y. F. Zhou, L. L. Li, T. S. Hu, Q. Wang, W. Shao, L. X. Rao, X. L. Xing and Q. X. Yang, Role of TiC nanocrystalline and interface of TiC and amorphous carbon on corrosion mechanism of titanium doped diamond-like carbon films: Exploration by experimental and first principle calculation, Appl. Surf. Sci., 2021, 542, 148740.

23 H. L. Wang, J. J. Tang, Y. J. Zhao and J. Du, First-principles study of Mg/Al2MgC2 heterogeneous nucleation interfaces, Appl. Surf. Sci., 2015, 355, 1091–1097.

24 P. J. Feibelman, Atomic arrangement and impurity bonding at a k-Al2O3 (001)/Al (771) interface: First-principles calculations, Phys. Rev. B: Condens. Matter Mater. Phys., 2007, 76, 235405.

25 L. X. Rao, H. Liu, W. Shao, T. S. Hu, X. L. Xing, X. J. Ren, Y. F. Zhou and Q. X. Yang, Investigation on the interface characteristic between TiN and diamond by first-principles calculation, Diamond Relat. Mater., 2020, 109, 108023.

26 L. Chen, Y. F. Li, B. Xiao, Q. L. Zheng, D. W. Yi, X. Q. Li and Y. M. Gao, A hierarchical high-throughput first principles investigation on the adhesion work, interfacial energy and tensile strength of NiTi2 (100)/a-Al2O3 (0001) interfaces, J. Mater. Res Technol., 2021, 14, 2932–2944.

27 G. Kresse and J. Furthmuller, Efficient iterative schemes for ab initio total-energy calculations using a plane-wave basis set, Phys. Rev. B: Condens. Matter Mater. Phys., 1996, 54, 11169.

28 P. E. Blo ¨chl, Projector augmented-wave method, Phys. Rev. B: Condens. Matter Mater. Phys., 1994, 50, 17953.

29 J. P. Perdew, K. Burke and M. Ernzerhof, Generalized gradient approximation made simple, Phys. Rev. Lett., 1996, 77, 3865.

30 H. J. Monkhorst and J. D. Pack, Special points for Brillouin zone integrations, Phys. Rev. B, 1976, 13, 5188.

31 R. R. Zope and Y. Mishin, Interatomic potentials for atomistic simulations of the Ti-Al system, Phys.Rev.B: Condens. Matter Mater. Phys., 2003, 68, 024102.

32 J. H. Tan, K. J. Zhu and J. H. Peng, First-principles simulation on structure-property of Ti-Al intermetallic compounds, J. Comput. Phys., 2017, 34, 365.

33 S. Sridharan, H. Nowotny and S. F. Wayne, Investigations within the quaternary system titanium-nickel-aluminium carbon, Monatsh. Chem., 1983, 114, 127–135.

34 Y. Koizumi, M. Mizuno, A. Sugihara, Y. Minamino and Y. Shirai, Effects of substitutional impurity Au and Si atoms on antiphase boundary energies in Ti3Al: A first principles study, Philos. Mag., 2010, 90, 3919–3934.

35 Z. X. Chen, H. S. Ding, R. R. Chen, S. Q. Liu, J. J. Guo and H. Z. Fu, An innovative method for the microstructural modification of TiAl alloy solidified via direct electric current application, J. Mater. Sci. Technol., 2019, 35, 23–28.

36 O. Ouadah, G. Merad and H. S. Abdelkader, Energetic segregation of B, C, N, O at the γ-TiAl/a2-Ti3Al interface via DFT approach, Vacuum, 2021, 186, 110045.

37 Y. Wei, Y. Zhang, G. H. Lu and H. B. Xu, Effects of transition metals in a binary-phase TiAl–Ti3Al alloy: From site occupancy, interfacial energetics to mechanical properties, Inter metallics, 2012, 31, 105–113.

38 J. C. Boettger, Nonconvergence of surface energies obtained from thin-film calculations, Phys. Rev. B: Condens. Matter Mater. Phys., 1994, 49, 16798.

39 H. Inui, A. Nakamura, M. H. Oh and M. Yamaguchi, High resolution electron microscope study of lamellar bound aries in Ti-rich TiAl polysynthetically twinned crystals, Ultramicroscopy, 1991, 39, 268–278.

40 D.J. Siegel, L. G. Hector Jr and J. B. Adams, Ab initio study of Al-ceramic interfacial adhesion, Phys. Rev. B: Condens. Mat ter Mater. Phys., 2003, 67, 092105.

41 M. Christensen, S. Dudiy and G. Wahnstro¨m, First principles simulations of metal-ceramic interface adhesion: Co/WC versus Co/TiC, Phys. Rev. B: Condens. Matter Mater. Phys., 2002, 65, 045408.

42 S. Hocker, H. Lipp, S. Schmauder, A. V. Bakulin and S. E. Kulkova, Ab initio investigation of Co/TaC interfaces, J. Alloys Compd., 2021, 853, 156944.

43 R. Topolnicki and R. Kucharczyk, Electronic properties of experimentally observed Pb/Ru (0 0 0 1) adsorbate structures: A DFT study, Appl. Surf. Sci., 2014, 304, 115–121.

44 A. D. Becke and K. E. Edgecombe, A simple measure of electron localization in atomic and molecular systems, J. Chem. Phys., 1990, 92, 5397–5403.

45 G. Y. Guo and H. H. Wang, Calculated elastic constants and electronic and magnetic properties of bcc, fcc, and hcp Cr crystals and thin films, Phys. Rev. B: Condens. Matter Mater. Phys., 2000, 62, 5136–5143.

46 W. Luo, D. Roundy, M. L. Cohen and J. W. Morris Jr, Ideal strength of bcc molybdenum and niobium, Phys. Rev. B: Condens. Matter Mater. Phys., 2002, 66, 094110.

47 P. Restuccia, G. Levita, M. Wolloch, G. Losi, G. Fatti, M. Ferrario and M. C. Righi, Ideal adhesive and shear strengths of solid interfaces: A high throughput ab initio approach, Comput. Mater. Sci., 2018, 154, 517–529.

Table 1 Parameters of bulk, surface and interface models for density functional calculations

System	Encut (eV)	K-points
Bulk γ-TiAl	500	5 × 5 × 5
Bulk α_2-Ti_3Al	500	9 × 9 × 9
γ-TiAl surface	500	5 × 5 × 1
α_2-Ti_3Al surface	500	9 × 9 × 1
γ-TiAl/α_2-Ti_3Al interface	500	9 × 9 × 1

Table 2 Surface energy of γ-TiAl(111) and α_2-Ti_3Al(0001) (J m^{-2})

Layer	4	5	6	7	8	9	10
γ-TiAl(111)	3.59	3.42	3.47	3.49	3.47	3.46	3.47
α_2-Ti_3Al(0001)	1.99	2.07	2.01	2.04	2.05	2.06	2.05

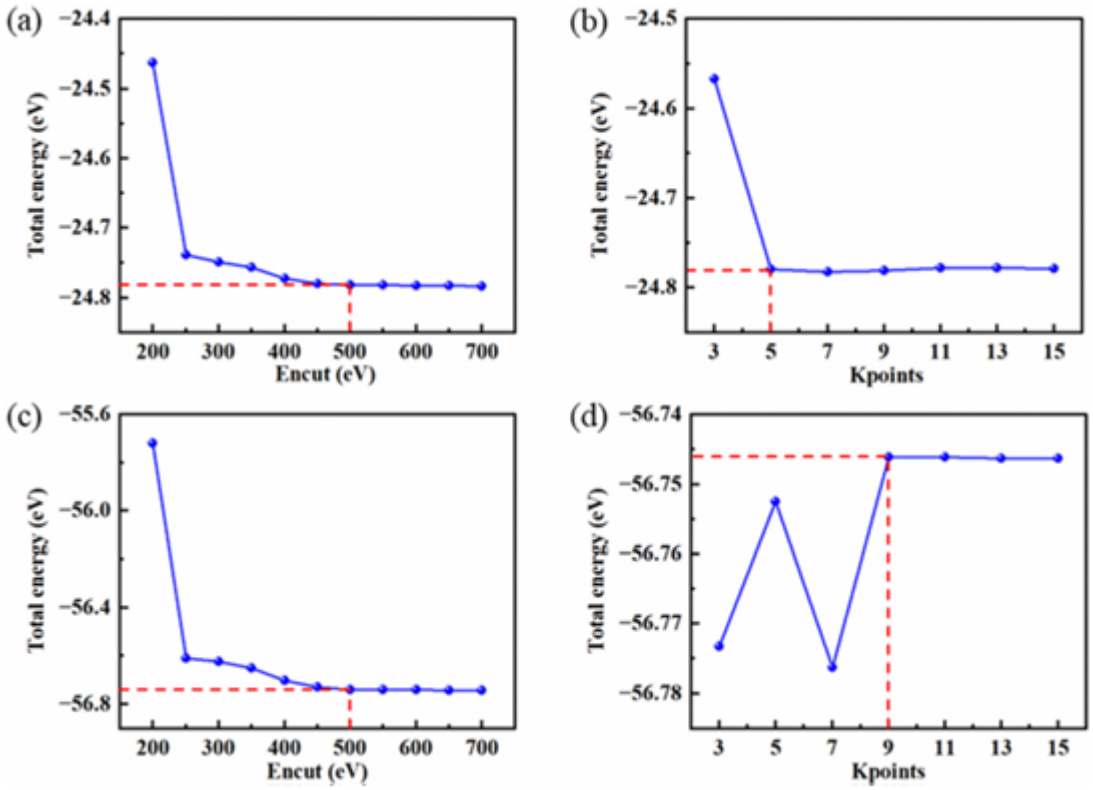

Fig. 1 Variation of energy with respect to encut and K-points. (a) γ-TiAl-encut; (b) γ-TiAl-K-points; (c) α_2-Ti_3Al-encut; and (d) α_2-Ti_3Al-K-points.

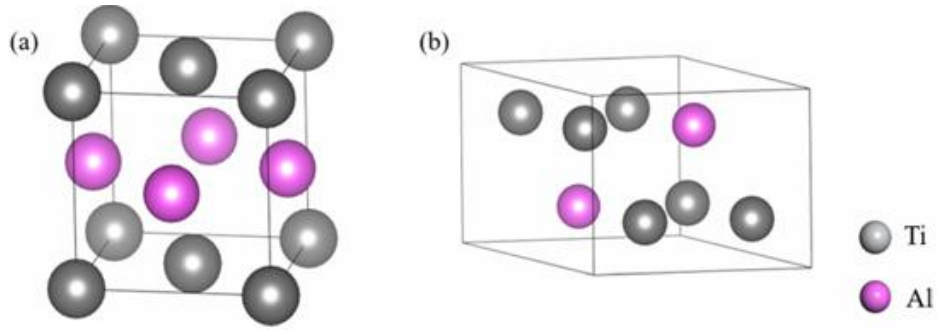

Fig. 2 Ideal crystal structures: (a) γ-TiAl and (b) α-Ti_3Al.

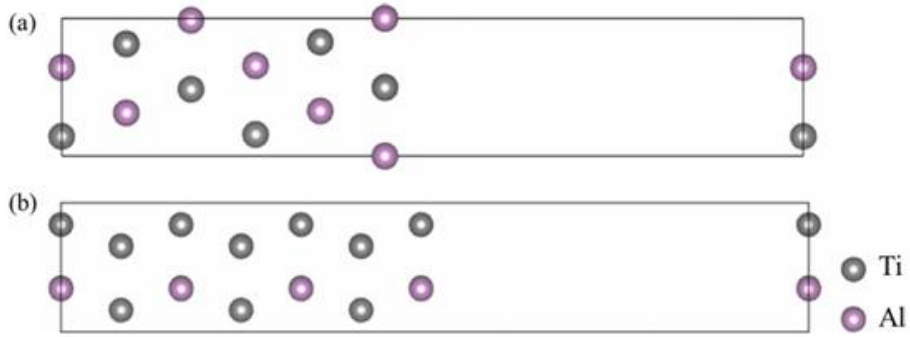

Fig. 3 Schematic of surface models of γ-TiAl(111) and α_2-Ti_3Al(0001). (a) γ-TiAl(111) and (b) α_2-Ti_3Al(0001).

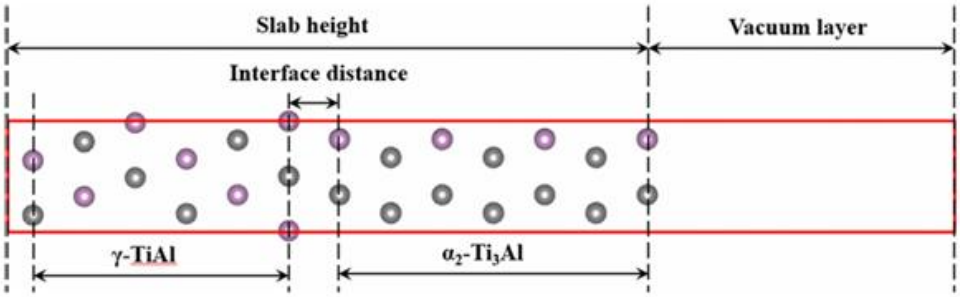

Fig. 4 Schematic of the interfacial model for γ-TiAl(111)/α_2-Ti_3Al(0001).

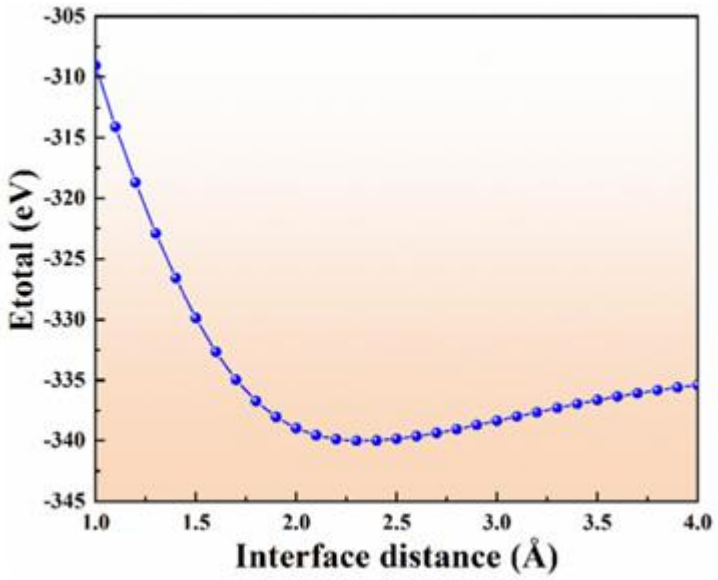

Fig. 5 Relationship between interfacial structural energy and interfacial spacing.

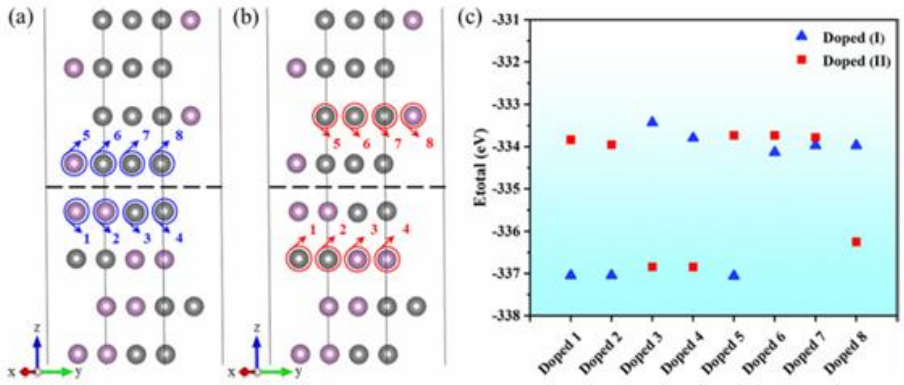

Fig. 6 Energy comparison chart for the La atom doped at different positions on the interface. (a) Doped points at the interface; (b) doped points at the sub-interface; and (c) energy comparison for different doped points

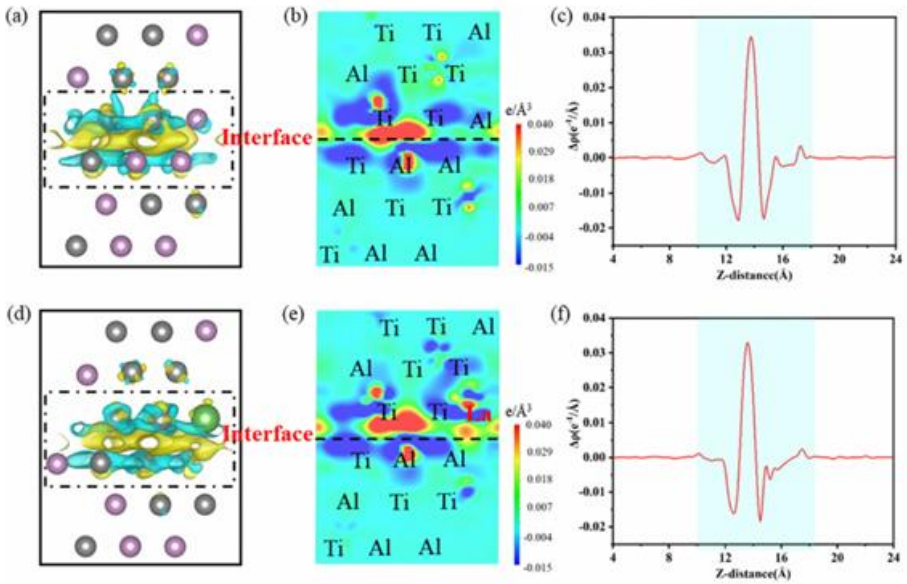

Fig. 7 Charge density diagrams of the interface before and after doping. (a) 3D differential charge density of the clear interface; (b) 2D differential charge density map of the clear interface; (c) planar averaged charge transfer along the z-axis for the clear interface; (d) 3D differential charge density of the doped interface; (e) 2D differential charge density map of the doped interface; and (f) planar averaged charge transfer along the z-axis for the doped interface.

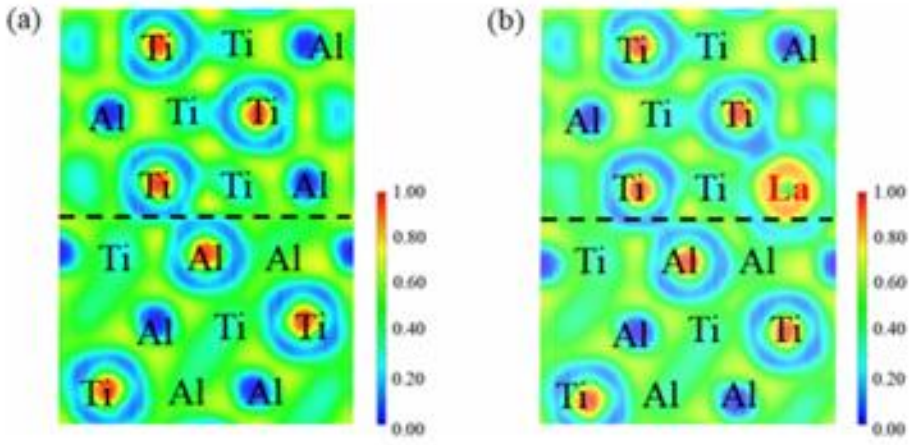

Fig. 8 Electron localization function. (a) Clear interface model and (b) doped interface model.

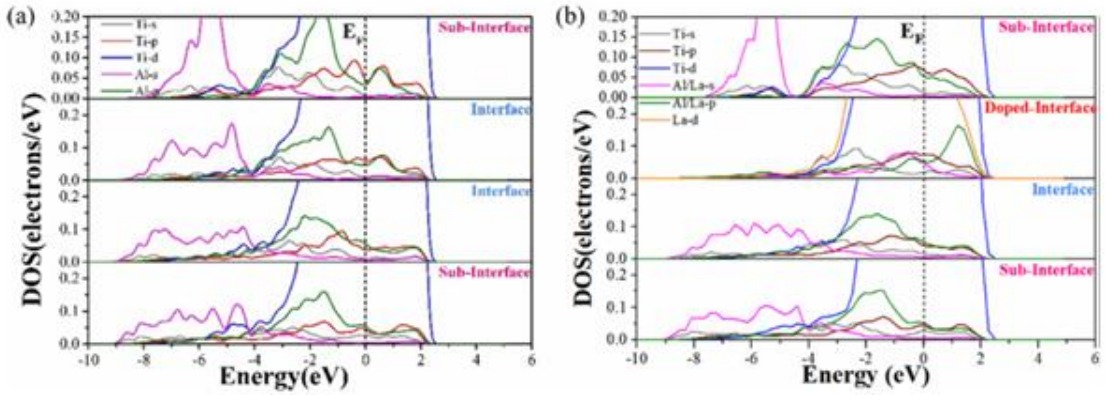

Fig. 9 Density of states (DOS) of interface layers. (a) Clear interface model and (b) doped interface model.

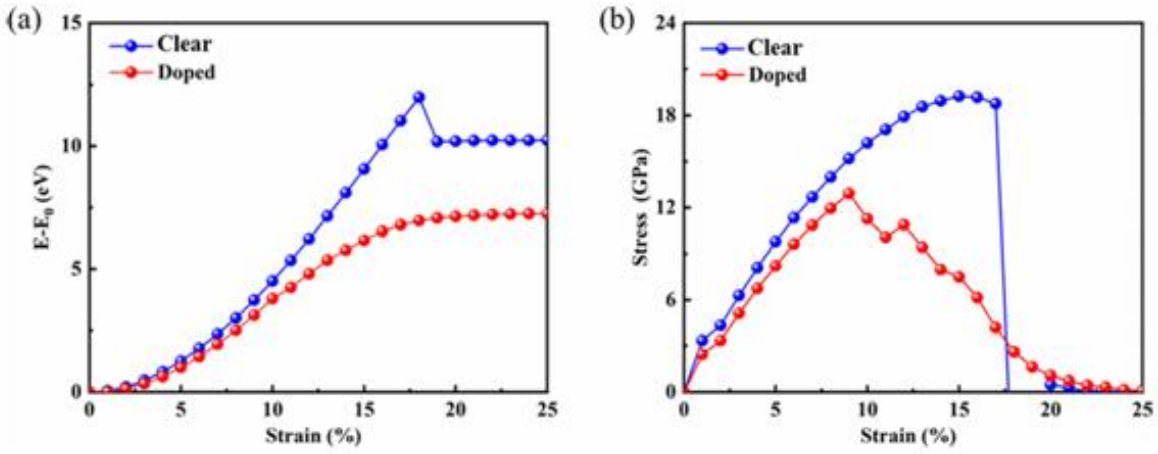

Fig. 10 Deformation energy and tensile stress curves. (a) Deformation energy–tensile strain and (b) tensile stress–tensile strain.

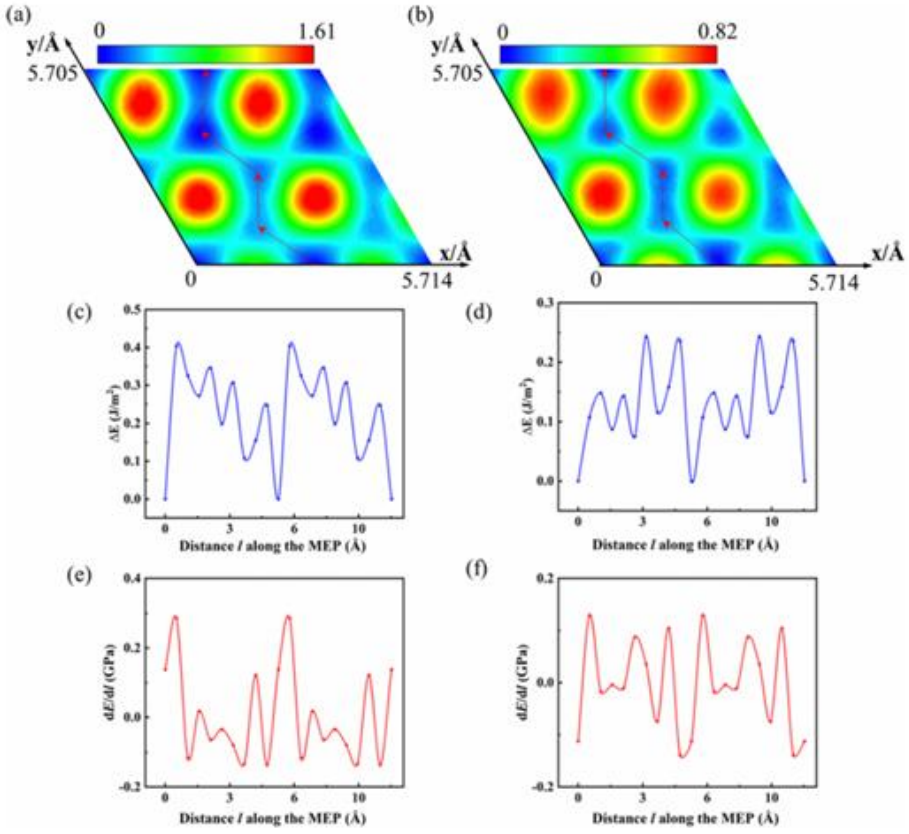

Fig. 11 Potential energy surfaces (PESs), potential energy curves (PECs) and their differential along the minimum energy path (MEP) of the γ-TiAl/α_2-Ti_3Al interface. (a) PES of a clear interface; (b) PES of a doped interface; (c) PEC along the MEP of a clear interface; (d) PEC along the MEP of a doped interface; (e) dE/dl along the MEP of a clear interface; and (f) dE/dl along the MEP of a doped interface.